

# Nuclear mass number dependence of inclusive production of $\omega$ and $\phi$ mesons in 12 GeV $p + A$ collisions

T. Tabaru,\* H. En'yo, R. Muto, M. Naruki, and S. Yokkaichi  
*RIKEN, 2-1 Hirosawa, Wako, Saitama 351-0198, Japan*

J. Chiba,<sup>†</sup> M. Ieiri, O. Sasaki, M. Sekimoto, and K. H. Tanaka  
*Institute of Particle and Nuclear Studies, KEK, 1-1 Oho, Tsukuba, Ibaraki 305-0801, Japan*

H. Funahashi, Y. Fukao, M. Kitaguchi, M. Ishino,<sup>‡</sup> H. Kanda,<sup>§</sup> S. Mihara,<sup>‡</sup> T. Miyashita, K. Miwa, T. Murakami, T. Nakura, F. Sakuma, M. Togawa, S. Yamada, and Y. Yoshimura  
*Department of Physics, Kyoto University, Kitashirakawa, Sakyo-ku, Kyoto 606-8502, Japan*

H. Hamagaki and K. Ozawa

*Center for Nuclear Study, Graduate School of Science, University of Tokyo, 7-3-1 Hongo, Tokyo 113-0033, Japan*

(Dated: February 9, 2020)

The inclusive production of  $\omega$  and  $\phi$  mesons is studied in the backward region of the interaction of 12 GeV protons with polyethylene, carbon, and copper targets. The mesons are measured in  $e^+e^-$  decay channels. The production cross sections of the mesons are presented as functions of rapidity  $y$  and transverse momentum  $p_T$ . The nuclear mass number dependences ( $A$  dependences) are found to be  $A^{0.710 \pm 0.021(\text{stat}) \pm 0.037(\text{syst})}$  for  $\omega$  mesons and  $A^{0.937 \pm 0.049(\text{stat}) \pm 0.018(\text{syst})}$  for  $\phi$  mesons in the region of  $0.9 < y < 1.7$  and  $p_T < 0.75$  GeV/ $c$ .

PACS numbers: 13.85.Ni, 13.85.Qk, 14.40.Cs

## I. INTRODUCTION

The modification of the vector meson spectral function in hot and/or dense matter is currently a hot subject in terms of spontaneous chiral symmetry breaking and partial restoration of the symmetry in nuclear matter. Currently, this is the focus of several experiments [1, 2, 3, 4]. The experiment KEK-PS E325 was performed to measure the vector meson spectral functions in dense matter, i.e., nucleus. Thus far, we have reported the signature of the mass modification of vector mesons [5, 6, 7]. These observations are fairly remarkable; hence, we also performed analyses to determine the absolute cross sections and nuclear mass number dependences of the production of these mesons in order to understand the underlying production mechanism.

The nuclear mass number dependence of the cross sections for the particle production is usually parameterized as

$$\sigma(A) = \sigma_0 A^\alpha \quad (1)$$

for a target nucleus with mass number  $A$ . When the collision energy  $\sqrt{s_{NN}}$  is sufficiently large, the parameter  $\alpha$  in the production of light mesons like pions or  $\rho$  mesons is about  $2/3$  [8, 9]. This can be interpreted by considering such productions to be dominated by primary collisions at the front surface of a target nucleus. Note that the mean free path of incident protons in a nucleus is as small as 1.4 fm. On the other hand,  $\alpha$  tends to unity in the case of hard reactions like the production of  $J/\psi$  at high energies,  $\sqrt{s_{NN}} \gtrsim 20$  GeV [9, 10, 11].

The present experiment was performed at  $\sqrt{s_{NN}} = 5.1$  GeV. At approximately this collision energy, measurements for  $\omega$  and  $\phi$  mesons with nuclear targets were not conducted.<sup>1</sup> Although higher energy like  $\sqrt{s_{NN}} \gtrsim 10$  GeV,  $\alpha$  for the  $\phi$  meson productions is reported to range from 0.81 to 0.96 [13, 14, 15], there is no reason to believe that these values are applicable at our energy.

A  $\phi$  meson is almost a pure  $s\bar{s}$  state. Therefore, the production of a  $\phi$  meson without other accompanying strange particles is suppressed by the Okubo-Zweig-Iizuka rule [16]. This results in the effective threshold energy being as high as  $\sqrt{s_{NN}} = 3.9$  GeV, which corresponds to  $2m_p + 2m_{s\bar{s}}$ , since two  $s\bar{s}$  pairs are effectively needed to realize the  $\phi$  production. Our collision energy is fairly close to this effective threshold. In addition, the importance of additional mechanisms for  $\phi$  meson production, such as an intrinsic  $s\bar{s}$  component in nucle-

\*Electronic address: tsugu@riken.jp

<sup>†</sup>Present Address: Department of Physics, Faculty of Science and Technology, Tokyo University of Science, 2641 Yamazaki, Noda, Chiba 378-8510, Japan

<sup>‡</sup>Present Address: ICEPP, University of Tokyo, 7-3-1 Hongo, Tokyo 113-0033, Japan

<sup>§</sup>Present Address: Physics Department, Graduate School of Science, Tohoku University, Sendai 980-8578, Japan

<sup>1</sup> An experiment using heavy ions was performed [12].

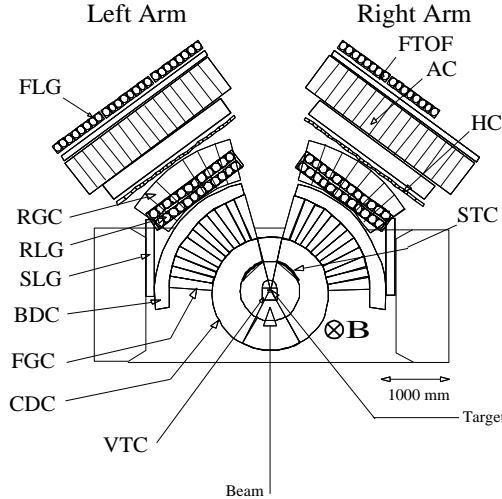


FIG. 1: Schematic view of the experimental setup, which is designed symmetrically with respect to the beam. The components of this setup are referred as left and right arms in this article.

ons [17] and  $\phi\rho\pi$  coupling [18, 19], have been suggested by theorists; however, they have thus far been sufficiently studied at our energy from an experimental viewpoint. Thus, to understand the production mechanism at our energy, basic measurements such as production cross sections and  $\alpha$  parameters are indispensable.

In this article, we present inclusive production cross sections and  $\alpha$  parameters of  $\omega$  and  $\phi$  mesons measured via the  $e^+e^-$  decay channels in 12 GeV  $p+p$ ,  $p+C$ , and  $p+Cu$  collisions. The results are compared to those from nuclear cascade simulation JAM [20], and the implications to production mechanisms are discussed.

## II. EXPERIMENT

The spectrometer was built in the EP1-B beam line at the 12 GeV proton synchrotron in KEK. The beam line was designed to deliver a 12 GeV primary proton beam with an intensity of up to  $4 \times 10^9$  protons per spill. The beam was extracted for 1.8 s with a repetition period of 4 s. The beam intensity was monitored with about 10% accuracy using ionization chambers [21] located downstream of the spectrometer.

Figure 1 shows a top view of the experimental setup. The spectrometer was designed to simultaneously measure  $e^+e^-$  and  $K^+K^-$  pairs. A dipole magnet and tracking devices were commonly used together with electron and kaon identification counters.

The magnet was operated at 0.71 T at the center of the dipole gap and provided 0.81 T·m of field integral for the tracking. The magnetic field map was calculated by the finite-element-analysis software TOSCA [22]. The calculated map agreed well with the measured map, and the difference was negligible when compared to the momentum resolution of this spectrometer. During the data

collection periods, the field strength was monitored with a nuclear-magnetic-resonance probe.

The targets were aligned inline along the beam axis at the center of the magnet. The target materials and configurations are shown in Table I. The typical beam size at the target was 2.0 mm in full-width half-maximum.

Three tracking devices—the vertex drift chamber (VTC), cylindrical drift chamber (CDC), and barrel drift chamber (BDC)—were used to determine the trajectories of the charged particles. In the present analysis, the momentum was determined using CDC and BDC. The momentum resolution  $\sigma_p$  was  $\sigma_p = \sqrt{(1.37\% \cdot p)^2 + 0.41\%^2 \cdot p}$  (GeV/c), where  $p$  is the momentum of a particle.

For the electron identification, two types of gas Čerenkov counters (FGC and RGC) and three types of lead glass calorimeters (SLG, RLG, and FLG) were employed. The gas Čerenkov counters were horizontally segmented into  $6^\circ$ . The radiator of the gas Čerenkov counters was isobutane at room temperature and atmospheric pressure. The refractive index is 1.00127 at the standard temperature and pressure, which corresponds to a momentum threshold of 2.26 GeV/c for charged pions. All lead glass detectors were built with SF6W [23] and were typically segmented to  $3.5^\circ$  horizontally. The typical energy resolution for 1 GeV electrons is 0.22 GeV. The acceptance for electrons ranged over  $\pm 12^\circ$  to  $\pm 90^\circ$  in the horizontal direction and  $-22^\circ$  to  $22^\circ$  in the vertical direction.

The counters for the kaon identification were start timing counters (STC), hodoscopes (HC), aerogel Čerenkov counters (AC), and time of flight counters (FTOF). The acceptance for kaons ranged over  $\pm 12^\circ$  to  $\pm 54^\circ$  in the horizontal direction, and from  $-6^\circ$  to  $6^\circ$  in the vertical directions. The three counters (STC, AC, and FTOF) were horizontally segmented to  $6^\circ$ , and HC was typically segmented horizontally to  $3^\circ$ . The time of flight (TOF) of charged particles was measured using STC and FTOF with a resolution of 0.36 ns and flight length of about 3.7 m. Kaons and pions were separated in a momentum range from 0.53 to 1.88 GeV/c using an aerogel with a refractive index of 1.034.

The electron trigger signal required a hit in FGC accompanied by a geometrical coincidence with RGC, SLG, or RLG. To select events containing  $e^+e^-$  pairs with large opening angles, both the left and the right arms were required to contain at least one  $e^+$  or  $e^-$  candidate. The typical efficiency of the trigger for the electron pairs in the acceptance was 92.4%.

The kaon trigger signal was obtained from the coincidence of STC, HC, and FTOF. The charged pion contamination was reduced by using AC as a veto trigger. Proton contamination was reduced by setting a TOF window for the kaons by using a rough momentum value calculated by combining the hits in STC, HC, and FTOF in the trigger.

The number of recorded events for electron data were  $7.41 \times 10^7$  and  $5.08 \times 10^8$  in 1999 and 2002, respectively. A detailed description of the spectrometer can be found

year	target	position (mm)	interaction length (%)	radiation length (%)	number of protons	trigger
1999	CH <sub>2</sub>	-48	0.111	0.195	$3.0 \times 10^{13}$	electron /kaon
	C	38	0.106	0.213		
	Cu	-7	0.0391	0.412		
2002	C	0	0.213	0.431	$3.2 \times 10^{14}$	electron
	Cu	$\pm 24, \pm 48$	$4 \times 0.0539$	$4 \times 0.565$		

TABLE I: Summary table for the targets, beams, and trigger modes used in the present analyses. In the 2002 run, four Cu targets were used.

in Ref. [24].

### III. DATA ANALYSIS

#### A. Analysis of $\omega$ and $\phi \rightarrow e^+e^-$ in $p + C$ and $p + Cu$ collisions

##### 1. Event reconstruction

The charged tracks were reconstructed from hit positions in the drift chambers by using the Runge-Kutta fitting method. After the tracks were reconstructed, tracks corresponding to momenta between 0.4 and 2.0 GeV/c were selected for further analyses. The lower limit in the momentum range was set based on the threshold of the trigger, whereas the upper was set in order to avoid pion contamination above the gas Čerenkov threshold.

Pairs of positive and negative tracks were required to satisfy the trigger condition. All the  $e^+$  and  $e^-$  candidates were reexamined so that an FGC hit association could be obtained with an RGC, SLG, or RLG association, depending on the location of the track. For candidates associated with lead glass calorimeters, the momentum ratio  $E/p$  should be larger than 0.5 for energy in the calorimeters to be obtained. We chose the value of 0.5 balancing the purity of  $e^+$  and  $e^-$  with the statistics of the present data. Figure 2 shows the distribution of the energy and momentum of the present data with FGC associations. In this figure, it is clearly seen that electrons range along the line of  $E = p$ . After an  $e^+e^-$  pair was detected, we simultaneously refit the  $e^+$  and  $e^-$  tracks by constraining them to have the same vertex point. Finally, we identified  $5.69 \times 10^5$  for the  $e^+e^-$  pairs.<sup>2</sup>

The track reconstruction efficiency was evaluated by both an eyescan and a detector simulation using GEANT4 [25]. By using the former method, the efficiency was found to be 67.2%. In the latter method, we em-

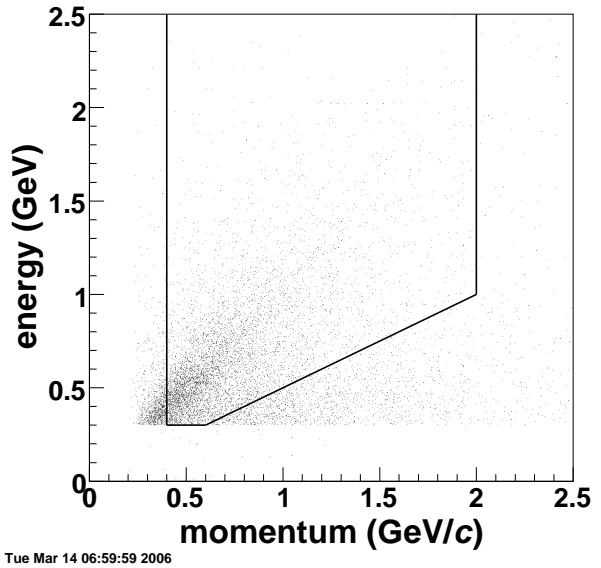


FIG. 2: The distribution of energy and momentum of the present data with FGC associations. The solid line shows the criterion of electron identification described in this article.

bedded the simulation tracks onto the real data in order to evaluate the efficiency considering track multiplicity. We averaged the efficiencies for each multiplicity with the track multiplicity distribution as the weight. By this method, the efficiency was found to be 78.0%. In order to combine the results of the two evaluations, we simply assumed the average to be the efficiency in the present analysis and considered half the difference as a systematic error. In addition, we calculated the probability of obtaining a good vertex point to be  $96.7 \pm 1.5\%$ . Therefore, the overall efficiency for detecting the  $e^+e^-$  pair was  $51.0 \pm 7.6\%$ .

##### 2. Corrections

Besides the tracking efficiency, several detector effects were evaluated and corrected as described below. The efficiencies of the electron identification counters were evaluated as a function of momentum by using pure electron samples from  $\gamma$  conversions and Dalitz decays. These

<sup>2</sup> In a further analysis, we used only events in which  $e^+$  went into the left arm and  $e^-$  went into the right arm because the number of events satisfying the opposite criterion comprised only 6% of the data.

electron samples were identified as a zero-mass peak in the  $e^+e^-$  spectra, and they were not required to participate in the trigger to avoid trigger bias. The obtained efficiencies were typically 85% for FGC, 86% for RGC, and 97% for the lead glass counters.

The energy losses of the tracks through the detectors were estimated by using GEANT4 simulation. Typically, the reconstructed momentum gave a value lower by 3 MeV/c for a 1 GeV/c electron due to the energy loss. The momentum difference was corrected track by track by using a correction table obtained by the simulation. It should be noted that this correction compensated only mean energy loss. For effects that cause an eventual large energy loss like bremsstrahlung, the corrections were carried out in a different manner, as described later.

The geometrical acceptances for the  $e^+e^-$  pairs were obtained as functions of the invariant mass,  $y$ , and  $p_T$  by the simulation. Isotropic decays to daughter pairs were assumed. The effects of the trigger, i.e., requirements of a geometrical correlation between the electron identification counters, were also considered. In order to obtain the yields of vector mesons, mass spectra were corrected for acceptance in the mass range above 0.55 GeV/c<sup>2</sup>. Below 0.55 GeV/c<sup>2</sup>, the correction was too large to evaluate reliable values. The obtained acceptances at the  $\omega$  and the  $\phi$  meson masses are tabulated in Fig. 3.

### 3. Spectrum decomposition

In Fig. 4, the left and the right panels show the spectra of the invariant mass of  $e^+e^-$  pairs in the range of  $0.9 < y < 1.7$  and  $p_T < 0.75$  GeV/c without and with the acceptance correction, respectively. The peaks of  $\omega$  and  $\phi$  are distinctly observed.

The  $e^+e^-$  mass spectra were fit and decomposed into  $\omega$  mesons;  $\phi$  mesons;  $\rho^0$  mesons; Dalitz decay components of  $\eta$ ,  $\omega$ , and  $\phi$  mesons; and the combinatorial background.

For the  $\omega$  and  $\phi$  meson shapes in the fit, the Breit-Wigner function

$$\frac{d\sigma}{dm} = \frac{N}{(m - m_0)^2 + \Gamma_{\text{tot}}^2/4} \quad (2)$$

convoluted with a Gaussian function for the experimental resolution was used. If the relativistic Breit-Wigner shape is used instead, the results do not change effectively. Here,  $\sigma$  is the cross section;  $m$ , the invariant mass of the  $e^+e^-$  pair;  $N$ , a normalization factor;  $m_0$ , the meson mass; and  $\Gamma_{\text{tot}}$ , the natural decay width. For the  $\rho^0$  meson shape, we used the relativistic Breit-Wigner shape

$$\frac{d\sigma}{dm} = \frac{N}{\left(m^2 - m_{\rho^0}^2\right)^2 + m^2 \Gamma_{\text{tot}}^2}, \quad (3)$$

instead of the Breit-Wigner function. To obtain the mass distribution in the spectrometer acceptance, we used the

GEANT4 simulation with an input momentum distribution of  $\rho^0$  mesons that was obtained using JAM. The  $e^+e^-$  invariant mass spectra from the Dalitz decays of  $\eta$ ,  $\omega$ , and  $\phi$  mesons were also obtained by the simulation. Their  $e^+e^-$  distributions were determined by following the vector meson dominance model given in Ref. [26] by using the mother meson distributions obtained by JAM. The combinatorial background shape was evaluated using an event mixing method.

The free parameters of the fit were the yields, the peak positions, and the mass resolutions of  $\omega$  and  $\phi$  mesons; the yields of  $\eta$  and  $\rho^0$  mesons; and the number of the background events. As mentioned earlier, the spectra were corrected in a mass range only above 0.55 GeV/c<sup>2</sup>. Therefore, below 0.55 GeV/c<sup>2</sup>, the uncorrected spectra were used in the fit mainly to accurately obtain the amount of the background. Although the fit region was from 0.20 GeV/c<sup>2</sup> to 1.2 GeV/c<sup>2</sup>, the mass regions from 0.600 to 0.765 GeV/c<sup>2</sup> and from 0.955 to 0.985 GeV/c<sup>2</sup> were excluded in order to avoid the effect of the excesses below the  $\omega$  and  $\phi$  peaks, which in other publications [5, 6, 7], we have claimed as the signal of the mass modification. In the present analysis, however, we did not assume any underlying physics for the excess, and we aimed only to obtain the yields of  $\omega$  and  $\phi$  mesons correctly, as discussed later.

The fit results are shown by thin solid lines in Fig. 4. The  $\chi^2$  over the number of degree of freedom were obtained as 157/152 and 192/152 for the  $p + C$  and  $p + Cu$  interactions, respectively.

After obtaining the raw yields of the  $\omega$  and  $\phi$  mesons by the fit, the correction for hard energy losses such as bremsstrahlung or a radiative tail was applied. The hard energy loss causes a low mass tail in the invariant mass distribution. The loss of the yield due to this tail could not be evaluated using the procedure described above; hence, we performed studies using the GEANT4 simulation. The yields of the tails with respect to the integrals of the Breit-Wigner peaks were found to be  $11.9 \pm 1.0\%$  for the  $\omega$  mesons and  $10.4 \pm 0.8\%$  for the  $\phi$  mesons. These values were simply added to the peak yields. The uncertainty of these corrections includes an ambiguity with respect to the cross sections of such hard energy losses in GEANT4.

By the fit procedure described above, the peak position and mass resolution of the  $\phi$  meson were obtained as  $1019 \pm 1$  MeV/c<sup>2</sup> and  $11.8 \pm 1.0$  MeV/c<sup>2</sup>, respectively. The peak position of the  $\phi$  meson is consistent with the values of Particle Data Group [27], and the mass resolution is consistent with the simulation value of 10.7 MeV/c<sup>2</sup>; however, the peak position of the  $\omega$  meson was found to be lower by 2.2 MeV/c<sup>2</sup>. The width of the omega mesons was also broader than that expected by the simulation.<sup>3</sup>

<sup>3</sup> If we take internal bremsstrahlung into account, the peak positions of both the  $\omega$  mesons and the  $\phi$  mesons agree with the

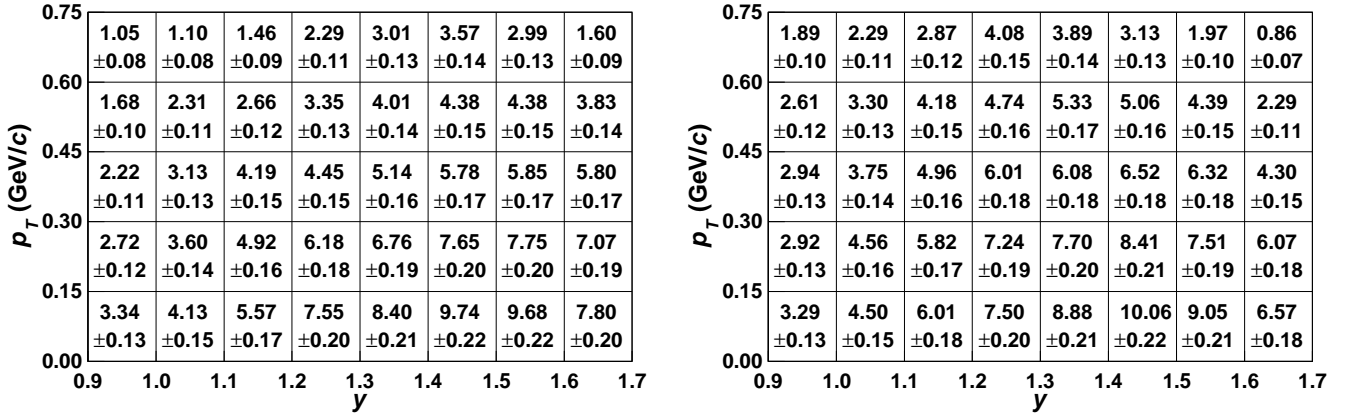


FIG. 3: Acceptances (%) for  $\omega$  meson mass (left) and  $\phi$  meson mass (right) as functions of  $y$  and  $p_T$ . The errors are statistical and are obtained from the simulation.

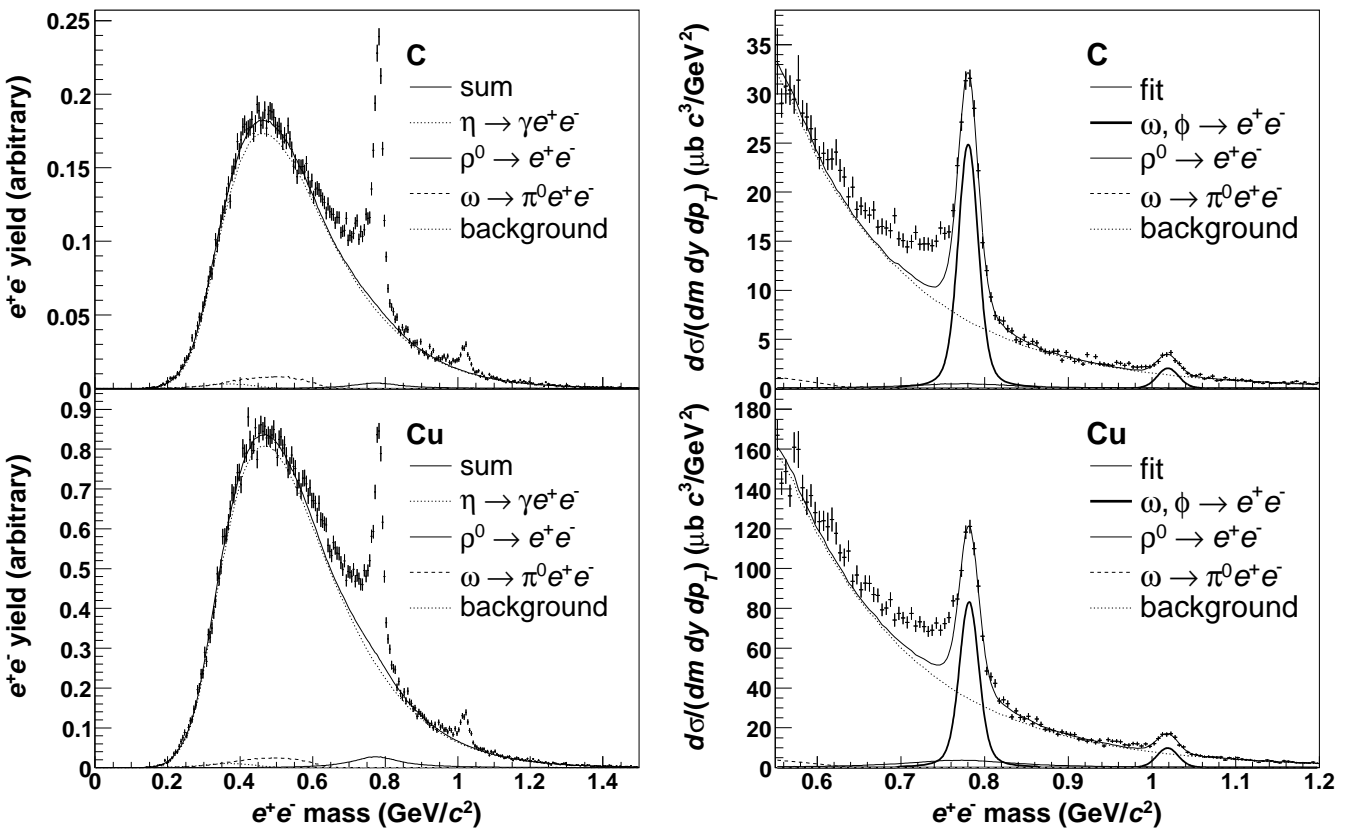


FIG. 4: The  $e^+e^-$  mass distributions of the acceptance-uncorrected data (left) and the corrected data (right) in the kinematic range of  $0.9 < y < 1.7$  and  $p_T < 0.75$  GeV/c. The lines in the left panels represent the backgrounds, Dalitz components,  $\rho^0$  components, and their sum. The amount of  $e^+e^-$  decays of  $\omega$  and  $\phi$  mesons is represented by thick solid lines in the right panels, and the thin solid lines represent the sum of all the components. The number of  $\phi$  meson Dalitz decays is negligibly small.

Here, we adopted a conservative approach in order to obtain the yield of unmodified  $\omega$  mesons by estimating the additional systematic error due to this peak shift. The error for the  $\omega$  meson yield was evaluated as 0.48% for a  $p + C$  interaction and 1.8% for a  $p + \text{Cu}$  interaction, which were obtained by forcing the peak position in the fit to the higher value of  $2.2 \text{ MeV}/c^2$ . The momentum scale and resolution were also verified using the  $K_s \rightarrow \pi^+ \pi^-$  data [7]. The measured peak position of  $K_s$  was  $496.8 \pm 0.3 \text{ MeV}/c^2$ , which was consistent with that of the simulation result,  $496.9 \text{ MeV}/c^2$ . The measured mass resolution of  $K_s$  was  $3.9 \pm 0.4 \text{ MeV}/c^2$ , which was expected to be  $3.5 \text{ MeV}/c^2$  by the simulation.

#### 4. Systematic errors

In addition to the uncertainties described previously, the following systematic uncertainties were studied to obtain the cross sections.

The uncertainty in the background shapes could be a source of the systematic error. The background was a result of uncorrelated pairs that were obtained from two independent Dalitz decays,  $\gamma$  conversions, or other meson decays. The background shape was obtained by an event mixing technique. In the mixing process, it is possible that the correlated  $e^+ e^-$  pairs from the decays of  $\rho^0$ ,  $\omega$ , and  $\phi$  mesons deform the estimated background shape; this could result in a systematic error. In order to estimate the systematic error, two methods were used in the event mixing. One was to use all electrons except for those belonging to the  $\omega$  and  $\phi$  meson mass regions, which are  $0.765$  to  $0.800 \text{ GeV}/c^2$  and  $0.995$  to  $1.035 \text{ GeV}/c^2$ , respectively. In the other method, we used all the pairs in the event mixing but with weights in order to obtain a self-consistent shape of the background. The weights were obtained as a function of the  $e^+ e^-$  mass as the ratio of the background shape to the real mass spectrum, and they were self-consistently determined by repeating the fit several times. We adopted the latter method to determine the background shape. The difference between the two methods was assigned as a systematic error. The difference in the yield of  $\omega$  mesons was 0.23% and that in  $\phi$  mesons was 0.60%.

The normalization and spectral shape of the combinatorial background were affected by all the other correlated  $e^+ e^-$  components since they were obtained by the fit. The systematic errors in the peak yield determination due to the ambiguity of the Dalitz decays of  $\eta$ ,  $\omega$ , and  $\phi$  mesons were evaluated by doubling or eliminating those yields and refitting the mass spectra. These systematic errors were found to be 0.62% and 0.85% for  $\omega$  and  $\phi$  mesons, respectively.

It was difficult to consider the uncertainty of the  $\rho^0$  shape, since the mass region from  $0.600$  to  $0.765 \text{ GeV}/c^2$  could not be represented by known sources, and the shape of the mass modification was not well understood. In this analysis, we simply considered the relativistic Breit-

	$\omega$	$\phi$
beam intensity	10	%
C target thickness	0.28%	
Cu target thickness	0.55%	
trigger electronics	3.8 %	
track reconstruction	14.9 %	
vertex reconstruction	1.5 %	
acceptance	1.23%	1.25%
hard energy loss	1.18%	0.94%
electron identification	2.92%	2.60%
background shape	0.23%	0.60%
mass scale for $p + C$	0.48%	
mass scale for $p + \text{Cu}$	1.83%	
Dalitz yield	0.62%	0.85%
$\rho^0$ from $p + C$	3.2 %	3.5 %
$\rho^0$ from $p + \text{Cu}$	7.6 %	5.5 %
total for $p + C$	19.0 %	19.0 %
total for $p + \text{Cu}$	20.3 %	19.5 %

TABLE II: Systematic uncertainties for  $\omega$  and  $\phi$  meson yields for the data taken in 2002.

Wigner shape for the  $\rho^0$  distribution and performed a fit by excluding the excess region. In order to evaluate the systematic error, we fixed the  $\rho^0$  yield at zero as an extreme case and reperformed the fit. In this fit, the  $\omega$  yield increased by 3.19% for the carbon target and 7.65% for the copper target; further, the  $\phi$  meson yield increased by 3.45% and 5.48% for each of the above targets, respectively. We considered these values as systematic errors due to the unknown  $\rho^0$  distribution. It should be noted that the  $\omega$  mesons can also be modified such that the  $\omega$  cross sections obtained in the present analysis are only for that component whose shape is consistent with the un-modified shape.

A possible cause of another error might lie in the efficiency estimations for electron identification. These uncertainties were evaluated by using the error bands of efficiency curves of electron identification counters and were obtained as 2.92% for  $\omega$  mesons and 2.60% for  $\phi$  mesons.

All the systematic errors are summarized in Table II. In the evaluation of the absolute cross section, the errors of the beam intensity, target thicknesses, and efficiency of the trigger electronics were also considered. In summary, the systematic errors for the cross sections for  $\omega$  mesons were 19.0% for the carbon target, and 20.3% for the copper target, and those of  $\phi$  mesons were 19.7% and 20.1%, respectively.

The systematic errors for the  $\alpha$  parameters are only due to the items that differ between carbon and copper targets. These are listed in Table III. In summary, the uncertainties for the  $\alpha$  parameters of  $\omega$  and  $\phi$  mesons were 5.2% and 1.9%, respectively.

	$\omega$	$\phi$
acceptance	1.47%	1.13%
target thickness	0.52%	0.39%
background shape	0.27%	0.54%
mass scale	1.13%	
Dalitz yield	0.37%	0.48%
$\rho^0$ yield	4.89%	1.25%
total	5.2 %	1.9 %

TABLE III: Systematic uncertainties for  $\alpha$  parameters of  $\omega$  and  $\phi$  mesons for the data taken in 2002.

### B. Extraction of the cross section in $p + p$ interaction

The target subtraction method was employed to obtain the cross section in  $p + p$  collisions; this was achieved by using the data taken in 1999. The production cross sections  $\sigma(p)$  in  $p + p$  collisions were calculated by the formula  $\sigma(p) = (\sigma(\text{CH}_2) - \sigma(\text{C}))/2$  in the region of  $0.9 < y < 1.7$  and  $p_T < 0.6 \text{ GeV}/c$ . The analysis was performed in almost the same manner as that for the data in 2002.

To minimize the uncertainty due to experimental differences between the 1999 and 2002 data, we normalized the yield of  $\omega$  mesons with carbon targets in the 1999 data to that in 2002 data and extracted the absolute cross sections in  $p + p$  collisions. Another uncertainty arose from the difference in the target thicknesses that were measured with an accuracy of 0.8%. We obtained 19.5% and 21.4% as the systematic uncertainty in  $p + p$  collisions for the  $\omega$  meson production and  $\phi$  meson production, respectively.

## IV. RESULT AND DISCUSSION

### A. Global feature of the obtained results

From the decay branching fractions listed in Table IV, the differential cross sections of the inclusive  $\omega$  meson production are obtained as  $13.92 \pm 0.33(\text{stat}) \pm 2.64(\text{syst}) \text{ mb}\cdot c/\text{GeV}$  and  $45.37 \pm 1.22(\text{stat}) \pm 9.21(\text{syst}) \text{ mb}\cdot c/\text{GeV}$  in  $p + \text{C}$  and  $p + \text{Cu}$  collisions in the region of  $0.9 < y < 1.7$  and  $p_T < 0.75 \text{ GeV}/c$ , respectively; further, those of  $\phi$  meson production are  $0.263 \pm 0.016(\text{stat}) \pm 0.050(\text{syst}) \text{ mb}\cdot c/\text{GeV}$  and  $1.255 \pm 0.068(\text{stat}) \pm 0.244(\text{syst}) \text{ mb}\cdot c/\text{GeV}$ , respectively.<sup>4</sup> The  $\alpha$  parameters of  $\omega$  and  $\phi$  mesons are obtained as  $0.710 \pm 0.021(\text{stat}) \pm 0.037(\text{syst})$  and  $0.937 \pm 0.049(\text{stat}) \pm 0.018(\text{syst})$ , respectively. The difference is

decay mode	branching fraction
$\omega \rightarrow e^+e^-$	$(6.96 \pm 0.15) \times 10^{-5}$
$\phi \rightarrow e^+e^-$	$(2.96 \pm 0.04) \times 10^{-4}$
$\phi \rightarrow K^+K^-$	$49.2^{+0.6\%}_{-0.7\%}$

TABLE IV: Branching fractions in the booklet of Particle Data Group [27].

$0.227 \pm 0.054(\text{stat}) \pm 0.041(\text{syst})$ , and it is statistically significant.

In order to compare the production cross sections in the  $e^+e^-$  decay channels with those in the  $K^+K^-$  decay channel and the previous measurement of  $12 \text{ GeV}/c$   $p + p \rightarrow \rho^0 X$  by Blobel *et al.* [28], the present data were extrapolated to the backward hemisphere—region of  $x_F < 0$  or  $y < 1.66$ —where  $x_F$  is Feynman's  $x$ . The production cross sections in the backward hemisphere are listed in Table V. The correction factors for this extrapolation from the measured regions— $0.9 < y < 1.7$  and  $p_T < 0.75 \text{ GeV}/c$ —to the backward hemisphere were calculated by using JAM, since the shapes of  $p_T$  and  $y$  spectra are consistent with the result of JAM calculation, as described later.

The cross sections of the inclusive  $\phi$  meson production in the  $K^+K^-$  decay channel are also listed in Table V. These were obtained from the previous analysis in this experiment [29, 30]. The  $\alpha$  parameter of the  $\phi$  meson production measured in the  $K^+K^-$  decay channel is obtained as  $1.01 \pm 0.09$  using the  $p + p$ ,  $p + \text{C}$ ,  $p + \text{Cu}$ , and  $p + \text{Pb}$  data in the spectrometer acceptance; this value is statistically consistent with the present  $e^+e^-$  analysis.

Figure 5 shows the cross sections in the backward hemisphere as a function of the nuclear mass number. The dotted lines represent the result of the JAM calculation and the solid lines represent the measured  $\alpha$  parameters. The  $\alpha$  parameters shown in the figure were 0.710, 0.937, and 1.01 for the data of  $\omega \rightarrow e^+e^-$ ,  $\phi \rightarrow e^+e^-$ , and  $\phi \rightarrow K^+K^-$ , respectively. It should be noted that these values were obtained from the data within the spectrometer acceptance before they were extrapolated to the backward hemisphere.

The previous measurement [28] yielded the total cross section of  $1.8 \pm 0.25 \text{ mb}$  for  $\rho^0$  mesons. By assuming a  $\rho^0/\omega$  ratio of  $1.0 \pm 0.2$ ,<sup>5</sup> we obtain the  $\omega$  meson production in the backward hemisphere as  $0.90 \pm 0.22 \text{ mb}$  for a comparison with the present measurement. The triangle in Fig. 5 represents the obtained value. The measured  $\omega$  meson production cross section in the present  $p + p$  collision data is consistent with their  $\rho^0$  cross section within the error.

<sup>4</sup> In this article, neither the effect of internal bremsstrahlung nor the uncertainty of the branching fractions is considered.

<sup>5</sup> The  $\rho^0/\omega$  ratio was measured by the reactions of  $p + p \rightarrow \rho^0 +$  charged particles and  $p + p \rightarrow \omega +$  charged particles.

	$\omega$ (mb)	$\phi (e^+e^-)$ (mb)	$\phi (K^+K^-)$ (mb)
H	$2.3 \pm 1.1 \pm 0.4$	$0.034 \pm 0.044 \pm 0.007$	$0.03 \pm 0.19 \pm 0.01$
C	$13.0 \pm 0.3 \pm 2.5$	$0.234 \pm 0.014 \pm 0.044$	$0.39 \pm 0.05 \pm 0.19$
Cu	$47.7 \pm 1.3 \pm 9.7$	$1.18 \pm 0.06 \pm 0.23$	$1.84 \pm 0.27 \pm 0.89$
Pb			$6.0 \pm 1.8 \pm 2.9$

TABLE V: Meson production cross section in the backward hemisphere. The first errors are statistic, where as the second errors are systematic. The data points are plotted in Fig. 5.

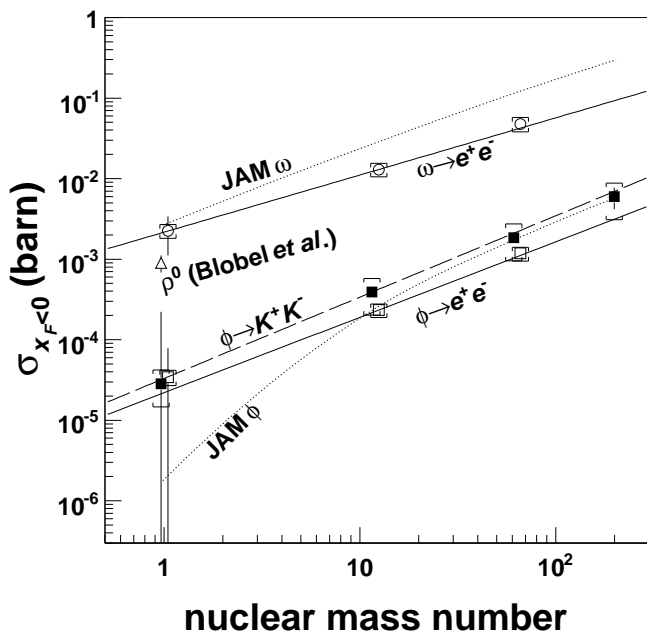


FIG. 5: Production cross section in the backward hemisphere as a function of mass number. The circles, open squares, and filled squares show the cross section of  $\omega$  mesons,  $\phi$  mesons measured in the  $e^+e^-$  decay channel, and those in the  $K^+K^-$  decay channel, respectively. The vertical lines represent the statistical errors, and the brackets represent the systematic errors. The previous  $p + p \rightarrow \rho^0 X$  measurement [28] is indicated by a triangle. The dotted lines represent the prediction by JAM simulation results. The solid lines represent the  $\alpha$  parameters (see text).

### B. Differential cross section of $\omega$ and $\phi$ production measured in $e^+e^-$ decays

In a region  $0.9 < y < 1.7$  and  $p_T < 0.75$  GeV/ $c$ , the differential cross sections of  $\omega$  and  $\phi$  mesons were obtained for each  $y$  or  $p_T$  bin, as shown in Fig. 6. These are also listed in Table VI.

The previous  $p + p \rightarrow \rho^0 X$  measurement [28] was plotted using triangles, as shown in Fig. 6. It should be noted that the data points were scaled by factors of 5.81 ( $= 12^{0.710}$ ) for clarity.

The distributions obtained by the JAM calculation are compared with the measurements in Fig. 6. The total cross sections obtained from the JAM calculation are

larger than that obtained from the data. Hence, they are scaled down by 47.6% for  $p + C \rightarrow \omega X$ , 41.0% for  $p + Cu \rightarrow \omega X$ , 97.9% for  $p + C \rightarrow \phi X$ , and 66.7% for  $p + Cu \rightarrow \phi X$ . The scale factors are determined as the ratio of the total cross sections in the acceptance between the data and JAM. The shapes of the differential cross sections of JAM are consistent with the present data, although the absolute cross sections are systematically larger than the data.

Figure 7 shows the  $\alpha$  parameters of  $\omega$  and  $\phi$  mesons obtained in the region of  $0.9 < y < 1.7$  and  $p_T < 0.75$  GeV/ $c$ . These are also listed in Table VI. The flat lines represent the averaged  $\alpha$  parameters with the errors shown in the left column. The dotted and dashed curves represent the results of JAM for  $p + C$  and  $p + Cu$  collisions. Although the  $\alpha$  parameters of the JAM calculation are significantly larger than those of the data, the difference between  $\omega$  and  $\phi$  mesons in the  $\alpha$  parameters is also seen in the JAM calculation.

### C. Discussion

An interesting characteristic is the difference in the  $y$  dependence between  $\omega$  and  $\phi$  meson production cross sections. Although the  $\omega$  production is independent of  $y$ , the  $\phi$  production increases in a smaller  $y$  region. In addition, the  $\alpha$  parameters of  $\omega$  and  $\phi$  meson production are different by  $0.227 \pm 0.054(\text{stat}) \pm 0.041(\text{syst})$ . This significant difference in the  $\alpha$  parameters confirms that the production mechanisms of  $\omega$  and  $\phi$  mesons are different.

One possible mechanism of  $\phi$  meson production is a hard reaction between incident and projectile nucleons. If the hard reaction is dominant like  $J/\psi$  production at higher energies,  $\alpha$  is expected to be around unity and independent of  $y$ . Further, the  $y$  distribution of the cross section is expected to be symmetric with respect to  $y_{CM}$ , which is not the case in the present  $\phi$  production data.

Another possible effect to explain the observed characteristics of the  $\alpha$  parameter and cross sections is the effect of secondary collisions in a target nucleus. In this case, no hard reaction is necessary. These effects are expected to increase in a smaller rapidity region for  $p + A$  interaction, and the cross sections and  $\alpha$  is expected to increase should be larger in the backward region.

Although the JAM does not reproduce the data quantitatively, it yields fairly similar shapes in the inclusive cross sections of  $\omega$  and  $\phi$  meson productions; further, it

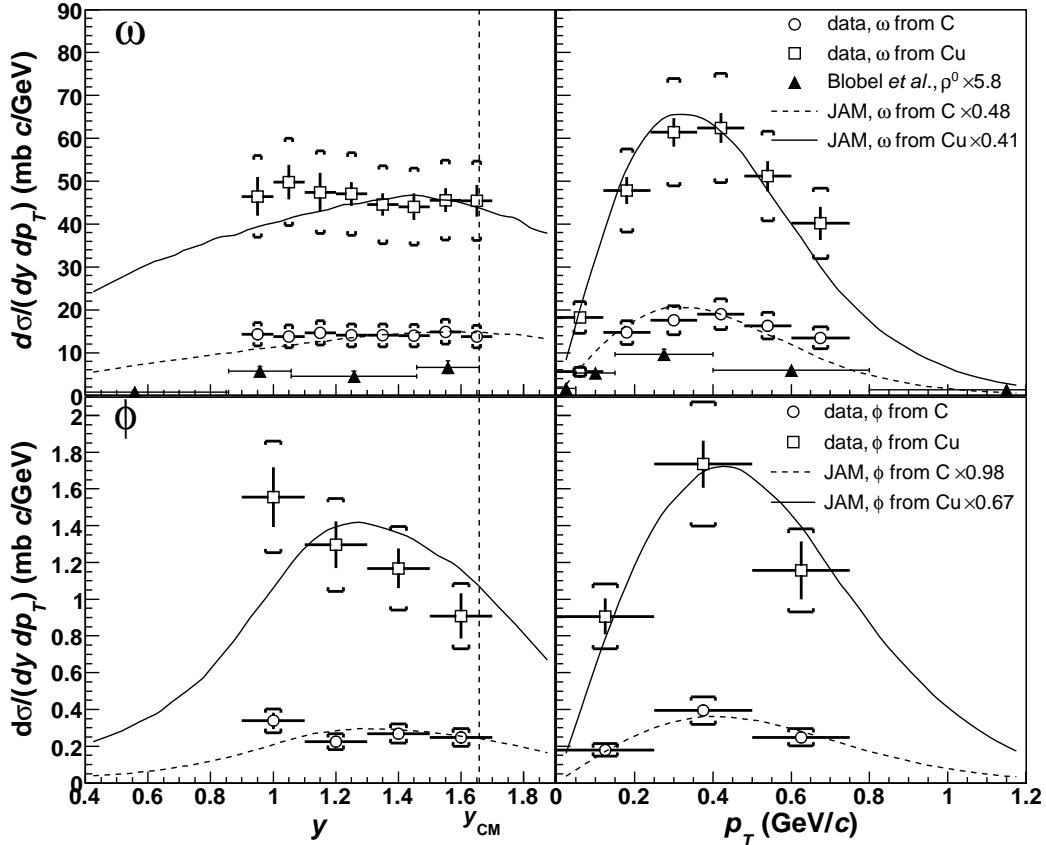


FIG. 6: Differential cross sections of  $\omega$  (top) and  $\phi$  (bottom) mesons as functions of  $y$  (left) or  $p_T$  (right). The statistical errors are represented by vertical bars, and the systematic errors are represented by brackets. The previous  $p + p \rightarrow \rho^0 X$  measurement [28] is indicated by triangles after scaling up with the nuclear mass number dependence obtained in the present analysis. The dashed and solid curves represent scaled cross sections of JAM in  $p + C$  and  $p + Cu$  collisions, respectively. The rapidity of the center of mass system is 1.66, as shown by  $y_{CM}$ . The data points are listed in Table VI.

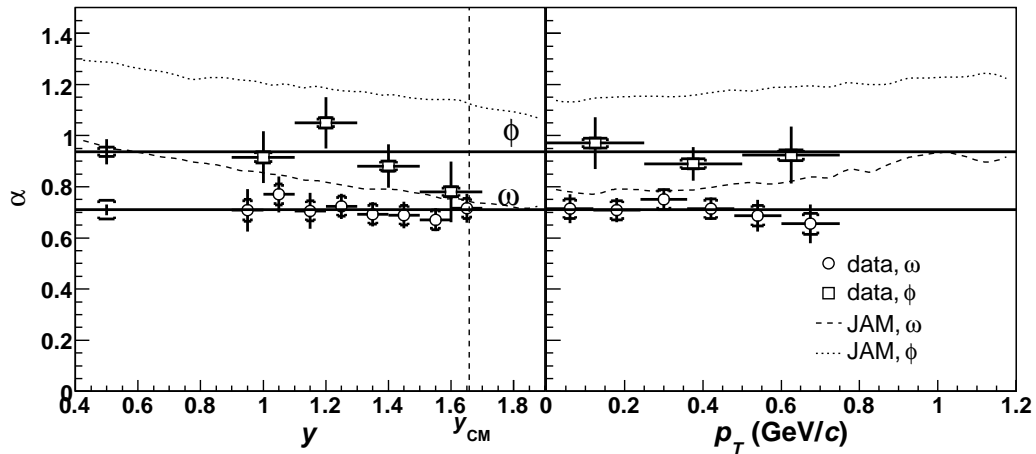


FIG. 7: The  $\alpha$  parameters of  $\omega$  (circle) and  $\phi$  (square) mesons as functions of  $y$  (left) or  $p_T$  (right). The statistical errors are represented by vertical bars and the systematic errors are represented by brackets. The horizontal lines represent the averaged  $\alpha$  parameters of  $\omega$  and  $\phi$  mesons with the errors indicated on the left side. The dotted and dashed curves represent the  $\alpha$  parameters of  $\phi$  and  $\omega$  mesons by JAM. The rapidity of the center of mass system is shown by  $y_{CM}$ . The data points are listed in Table VI.

		$\omega$ from C (mb $c/\text{GeV}$ )			$\omega$ from Cu (mb $c/\text{GeV}$ )			$\alpha$
$y$	0.9 –1.0	14.3	$\pm$ 1.4	$\pm$ 2.7	46.5	$\pm$ 4.5	$\pm$ 9.5	$0.708 \pm 0.083 \pm 0.042$
	1.0 –1.1	13.8	$\pm$ 1.2	$\pm$ 2.6	49.8	$\pm$ 4.0	$\pm$ 10.2	$0.770 \pm 0.070 \pm 0.041$
	1.1 –1.2	14.6	$\pm$ 1.0	$\pm$ 2.8	47.4	$\pm$ 4.5	$\pm$ 9.7	$0.706 \pm 0.071 \pm 0.040$
	1.2 –1.3	14.1	$\pm$ 0.8	$\pm$ 2.7	47.0	$\pm$ 2.8	$\pm$ 9.6	$0.724 \pm 0.049 \pm 0.039$
	1.3 –1.4	14.0	$\pm$ 0.8	$\pm$ 2.7	44.5	$\pm$ 2.6	$\pm$ 9.1	$0.693 \pm 0.048 \pm 0.039$
	1.4 –1.5	14.0	$\pm$ 0.7	$\pm$ 2.7	44.1	$\pm$ 3.1	$\pm$ 9.0	$0.689 \pm 0.052 \pm 0.039$
	1.5 –1.6	14.9	$\pm$ 0.6	$\pm$ 2.8	45.6	$\pm$ 2.8	$\pm$ 9.3	$0.671 \pm 0.045 \pm 0.038$
	1.6 –1.7	13.8	$\pm$ 0.6	$\pm$ 2.6	45.4	$\pm$ 3.7	$\pm$ 9.2	$0.716 \pm 0.056 \pm 0.039$
$p_T$ (GeV/ $c$ )	0.00–0.12	5.6	$\pm$ 0.4	$\pm$ 1.1	18.2	$\pm$ 1.2	$\pm$ 3.7	$0.714 \pm 0.057 \pm 0.038$
	0.12–0.24	14.7	$\pm$ 0.6	$\pm$ 2.8	47.8	$\pm$ 3.2	$\pm$ 9.7	$0.709 \pm 0.047 \pm 0.038$
	0.24–0.36	17.6	$\pm$ 0.8	$\pm$ 3.4	61.4	$\pm$ 3.3	$\pm$ 12.5	$0.750 \pm 0.042 \pm 0.039$
	0.36–0.48	19.0	$\pm$ 0.9	$\pm$ 3.6	62.4	$\pm$ 3.5	$\pm$ 12.7	$0.714 \pm 0.044 \pm 0.038$
	0.48–0.60	16.3	$\pm$ 1.3	$\pm$ 3.1	51.2	$\pm$ 3.5	$\pm$ 10.4	$0.687 \pm 0.063 \pm 0.040$
	0.60–0.75	13.5	$\pm$ 1.1	$\pm$ 2.6	40.2	$\pm$ 3.8	$\pm$ 8.2	$0.655 \pm 0.075 \pm 0.041$
	$0.9 < y < 1.7, p_T < 0.75 \text{ GeV}/c$	13.92	$\pm$ 0.33	$\pm$ 2.64	45.37	$\pm$ 1.22	$\pm$ 9.21	$0.710 \pm 0.021 \pm 0.037$
		$\phi$ from C			$\phi$ from Cu			$\alpha$
$y$	0.9 –1.1	$0.338 \pm 0.045 \pm 0.065$			1.56	$\pm$ 0.16	$\pm$ 0.30	$0.916 \pm 0.101 \pm 0.022$
	1.1 –1.3	$0.225 \pm 0.031 \pm 0.043$			1.30	$\pm$ 0.13	$\pm$ 0.25	$1.050 \pm 0.101 \pm 0.020$
	1.3 –1.5	$0.269 \pm 0.028 \pm 0.051$			1.17	$\pm$ 0.11	$\pm$ 0.23	$0.881 \pm 0.084 \pm 0.020$
	1.5 –1.7	$0.248 \pm 0.036 \pm 0.047$			0.91	$\pm$ 0.12	$\pm$ 0.18	$0.780 \pm 0.119 \pm 0.019$
$p_T$ (GeV/ $c$ )	0.00–0.25	$0.180 \pm 0.023 \pm 0.034$			0.91	$\pm$ 0.10	$\pm$ 0.18	$0.971 \pm 0.101 \pm 0.019$
	0.25–0.50	$0.394 \pm 0.032 \pm 0.075$			1.73	$\pm$ 0.13	$\pm$ 0.34	$0.890 \pm 0.066 \pm 0.019$
	0.50–0.75	$0.248 \pm 0.031 \pm 0.047$			1.16	$\pm$ 0.16	$\pm$ 0.23	$0.924 \pm 0.111 \pm 0.021$
$0.9 < y < 1.7, p_T < 0.75 \text{ GeV}/c$		$0.263 \pm 0.016 \pm 0.050$			1.255	$\pm$ 0.068	$\pm$ 0.244	$0.937 \pm 0.049 \pm 0.018$

TABLE VI: Differential production cross section in  $0.9 < y < 1.7$  and  $p_T < 0.75 \text{ GeV}/c$  measured via  $e^+e^-$  decay channel. The first errors are statistical and the second are systematic. The data points are plotted in Figs. 6 and 7.

also predicts the difference between the  $\alpha$  parameters of these mesons. In the JAM calculation, more than 90% of the  $\phi$  mesons are produced by secondary collisions primarily between non-strange mesons and nucleons in a target nucleus, while  $\omega$  mesons are produced both in primary and secondary reactions. For example, 30% and 50% of the  $\omega$  mesons are produced in cases of 12 GeV  $p + C$  and  $p + \text{Cu}$  reactions, respectively. These differences in the production mechanism cause the differences between the  $\omega$  and  $\phi$  mesons in the  $y$  dependence of the production cross sections and the  $\alpha$  parameters in the JAM simulation.

In summary, we measured the inclusive differential cross sections of the  $\omega$  and  $\phi$  meson production in  $p + A$  collisions in the backward region. The mass number dependence of these productions differs significantly. Com-

parisons with the nuclear cascade simulation suggest that  $\phi$  mesons are produced mainly in secondary collisions.

### Acknowledgments

We are grateful to all of the staff members of KEK-PS, especially the beam channel group, for their helpful support. This work was partly funded by the Japan Society for the Promotion of Science, RIKEN Special Post doctoral Researchers Program, and a Grant-in-Aid for Scientific Research from the Japan Ministry of Education, Culture, Sports, Science and Technology (MEXT). Finally, we also thank the staff members of RIKEN super combined cluster system and RIKEN-CCJ.

---

[1] G. Agakishiev et al., Eur. Phys. J. **C4**, 231 (1998).  
[2] G. M. Huber et al. (TAGX), Phys. Rev. **C68**, 065202 (2003), nucl-ex/0310011.  
[3] K. Suzuki et al., Phys. Rev. Lett. **92**, 072302 (2004), nucl-ex/0211023.  
[4] D. Trnka et al. (CBELSA/TAPS), Phys. Rev. Lett. **94**, 192303 (2005), nucl-ex/0504010.  
[5] K. Ozawa et al. (E325), Phys. Rev. Lett. **86**, 5019 (2001), nucl-ex/0011013.  
[6] M. Naruki et al. (E325), Phys. Rev. Lett. **96**, 092301 (2006), nucl-ex/0504016.  
[7] R. Muto et al. (E325) (2005), nucl-ex/0511019.  
[8] M. Ono, J. Kishiro, S. Mikamo, A. Kusumegi, and T. Ishizuka, Phys. Lett. **B84**, 515 (1979).  
[9] M. Binkley et al., Phys. Rev. Lett. **37**, 571 (1976).  
[10] B. Alessandro et al. (NA50), Eur. Phys. J. **C33**, 31 (2004).  
[11] U. Husemann (HERA-B), Nucl. Phys. Proc. Suppl. **142**,

104 (2005), hep-ex/0408110.

[12] B. B. Back et al. (E917), Phys. Rev. **C69**, 054901 (2004), nucl-ex/0304017.

[13] C. Daum et al. (ACCMOR), Z. Phys. **C18**, 1 (1983).

[14] R. Bailey et al. (ACCMOR), Z. Phys. **C24**, 111 (1984).

[15] A. N. Aleev et al. (BIS-2), Czech. J. Phys. **42**, 11 (1992).

[16] S. Okubo, Phys. Lett. **5**, 165 (1963).

[17] J. R. Ellis, M. Karliner, D. E. Kharzeev, and M. G. Sapozhnikov, Nucl. Phys. **A673**, 256 (2000), hep-ph/9909235.

[18] S. von Rotz, M. P. Locher, and V. E. Markushin, Eur. Phys. J. **A7**, 261 (2000), hep-ph/9912359.

[19] K. Nakayama, J. Haidenbauer, and J. Speth, Phys. Rev. **C63**, 015201 (2001), nucl-th/0008047.

[20] Y. Nara, N. Otuka, A. Ohnishi, K. Niita, and S. Chiba, Phys. Rev. **C61**, 024901 (2000), nucl-th/9904059, URL <http://quark.phy.bnl.gov/~ynara/jam/>.

[21] Y. Sugaya et al., Nucl. Instrum. Meth. **A368**, 635 (1996).

[22] J. Simkin and C. W. Trowbridge, Rutherford Laboratory, RL-79-097 (1979), URL <http://www.vectorfields.co.uk/>.

[23] S. Kawabata et al., Nucl. Instrum. Meth. **A270**, 11 (1988).

[24] M. Sekimoto et al. (E325), Nucl. Instrum. Meth. **A516**, 390 (2004).

[25] S. Agostinelli et al. (GEANT4), Nucl. Instrum. Meth. **A506**, 250 (2003), URL <http://wwwasd.web.cern.ch/wwwasd/geant4/geant4.html>.

[26] A. Faessler, C. Fuchs, and M. I. Krivoruchenko, Phys. Rev. **C61**, 035206 (2000), nucl-th/9904024.

[27] K. Hagiwara et al. (Particle Data Group), Phys. Rev. **D66**, 010001 (2002).

[28] V. Blobel et al. (Bonn-Hamburg-Munich), Phys. Lett. **B48**, 73 (1974).

[29] S. Yokkaichi, doctor thesis, Memoirs of the Faculty of Science, Kyoto University, Series of Physics, Astrophysics, Geophysics and Chemistry **41**, No.1, Article 3 (2000).

[30] M. Ishino, doctor thesis, Memoirs of the Faculty of Science, Kyoto University, Series of Physics, Astrophysics, Geophysics and Chemistry **42**, No.1, Article 1 (2000).